Roving Multiple Camera Array with Structure-from-Motion for Coastal Monitoring

Author Information

Dr Samantha Godfrey,[1] Professor James Cooper,[1] and Professor Andrew J Plater.[1*]

[1] School of Environmental Sciences, University of Liverpool, Liverpool, UK

*Correspondence to: Professor Andrew J Plater, School of Environmental Sciences, Roxby Building, University of Liverpool, Liverpool, L69 7ZT, UK. E-mail: gg07@liverpool.ac.uk

Abstract

Regular monitoring is essential for vulnerable coastal locations such as areas of landward retreat. However, for coastal practitioners, surveying is limited by budget, specialist personnel/equipment and weather. In combination structure-from-motion and multi-view stereo (SfM-MVS) has helped to improve accessibility to topographic data acquisition. Pole-mounted cameras with SfM-MVS have gained traction but to guarantee coverage and reconstruction quality, greater understanding is required on camera position and interaction. This study uses a multi-camera array for image acquisition and reviews processing procedures in Agisoft Photoscan (Metashape). The camera rig was deployed at three sites and results verified against a terrestrial laser scanner (TLS) and independent precision estimates. The multi-camera approach provided effective image acquisition ~11 times faster than the TLS. Reconstruction quality equalled (>92% similarity) the TLS, subject to processing parameters. A change in image alignment parameter demonstrated significant influence on deformation, reducing reprojection error by~ 94%. A lower densification parameter ('High') offered results ~4.39% dissimilar from the TLS at 1/8th of the processing time of other parameters. Independent precision estimates were <8.2mm for *x, y* and *z* dimensions. These findings illustrate the potential of multi-camera systems and the influence of processing on point cloud quality and computation time.

KEYWORDS: camera array; camera rig; coastal monitoring; coastal recession; SfM-MVS processing parameters; structure-from-motion photogrammetry; 3D reconstruction

1. Introduction

Coastal monitoring is an essential part of coastal protection, and repeat surveys offer insights into the effect of hydrodynamics on local geomorphology. Regular and impromptu surveying enables understanding of erosion rates, storm response and longer-term trends (Harley et al., 2011), and is important for the mitigation and prevention of flooding and erosion events.

For coastal researchers and managers, increasing the frequency of surveys for coastal recession assessment can be complex and limited by factors such as budget, availability of specialist personnel or weather conditions. Development of SfM-MVS, a low-cost and flexible 3D reconstruction technique, has become an increasingly effective method for acquiring topographic data and has shown to provide results comparable to 'industry standard' TLS surveys (Westoby et al. 2018; Del Rio et al., 2020). TLS deployment is common practice for monitoring coastal recession; however, surveys can be extremely costly, skilled operators are required, and survey times can be long (Dewez et al., 2013; Rosser et al., 2013; Letortu et al., 2018; Westoby et al., 2018).

SfM-MVS was derived from traditional photogrammetry, enabling 3D scene geometry to be reconstructed from 2D images. The quality of SfM-MVS reconstruction is highly dependent upon the effectiveness of the image acquisition scheme. The flexibility of SfM-MVS has fuelled development of novel applications and data acquisition schemes adapted to specific budgets, scales or environments. A variety of platforms have been utilised for monitoring coastal environments such as unmanned aerial vehicles (UAV) (e.g. Casella et al., 2020), poles (e.g. Pikelj et al., 2018), kites (e.g. Duffy et al., 2018) and hand-held cameras (e.g. James and Robson 2012). UAVs have become a popular platform for image acquisition but not all coastal researchers have the expertise or budget to use UAVs, and coastal flights are increasingly subject to tightened regulations (JNCC, 2019).

The use of terrestrial pole-mounted cameras with SfM-MVS is less restricted, making them useful in coastal settings. Single cameras with telescopic poles or cranes has proven an effective image acquisition method for geomorphic change (Rossi, 2018; Visser et al., 2019). Recent developments in commercial GNSS systems (Leica GS18) containing a very low-resolution camera (1 MP) for 3D reconstructions shows the desire for adaptable image acquisition techniques, highlighting future avenues of development for pole-mounted cameras with SfM-MVS. For this approach to be deployed, two significant operational challenges need to be addressed: first, establishing the camera's field of view (FOV) during image capture; secondly, optimising the overlap and interaction of images in the network because the camera's position and orientation are harder to verify and maintain. These issues make it challenging to guarantee coverage of a site, thus requiring a significant degree of pre-planning for image acquisition to reduce the risk of inadequate results (Wessling, Maurer and Krenn-Leeb, 2014; Eltner et al., 2016).

There is an opportunity to provide an alternative, efficient, approach to SfM-MVS image acquisition and, therefore, processing which would enable regular surveys of coastal recession. The use of a pole mounted array of cameras, along with systematic and pre-determined guidelines for image acquisition, would define image interaction before deployment. Moreover, the identification of optimal processing parameters for this setup may reduce computational cost whilst aiding the accurate reconstruction of the point cloud.

The aim of this paper is to explore this potential by designing and testing a bespoke multi-camera rig that can achieve scene reconstruction similar to a TLS. The developed camera array is deployed at three coastal recession sites (< 2 m height). The objectives are three-fold: 1. to test the degree to which acquiring images in this way can speed up data acquisition in comparison to a TLS, without over- or under-representing an area of the survey; 2. to optimise SfM-MVS processing parameters to produce reconstructions similar to that of a TLS; and 3. to assess the overall reconstruction quality compared to a TLS, a benchmark of survey performance. This research builds on the work of Godfrey et al. (2020) by employing multiple synchronised cameras on a roving rig over larger scales and investigates the role software parameters play on computational processing and deformation reduction at sites with a linear image acquisition. The goal is to provide a systematic and reliable approach to using SfM-MVS for monitoring landward retreat which will reduce data gaps and provide an option for less experienced users on lower budgets and in highly restricted environments.

1.1 **Study Sites**

A camera rig was used to survey three sites of landward retreat: Crosby, Thurstaston and Silverdale on the north-west coast of England, UK. Each site had different scale, sediment composition, vegetation cover and had been exposed to different hydrodynamic conditions, thus providing evidence of research applicability.

1.1.1 Crosby

Crosby is located north of the Mersey Estuary in Liverpool Bay, North-West England, UK (Figure 1a). The coastline is susceptible to some of the highest surge conditions in the UK owing to the shallow nature of the north-eastern Irish Sea. Crosby has a macro-tidal environment with a mean spring tidal range of ~ 8 m (Plater & Grenville, 2010).

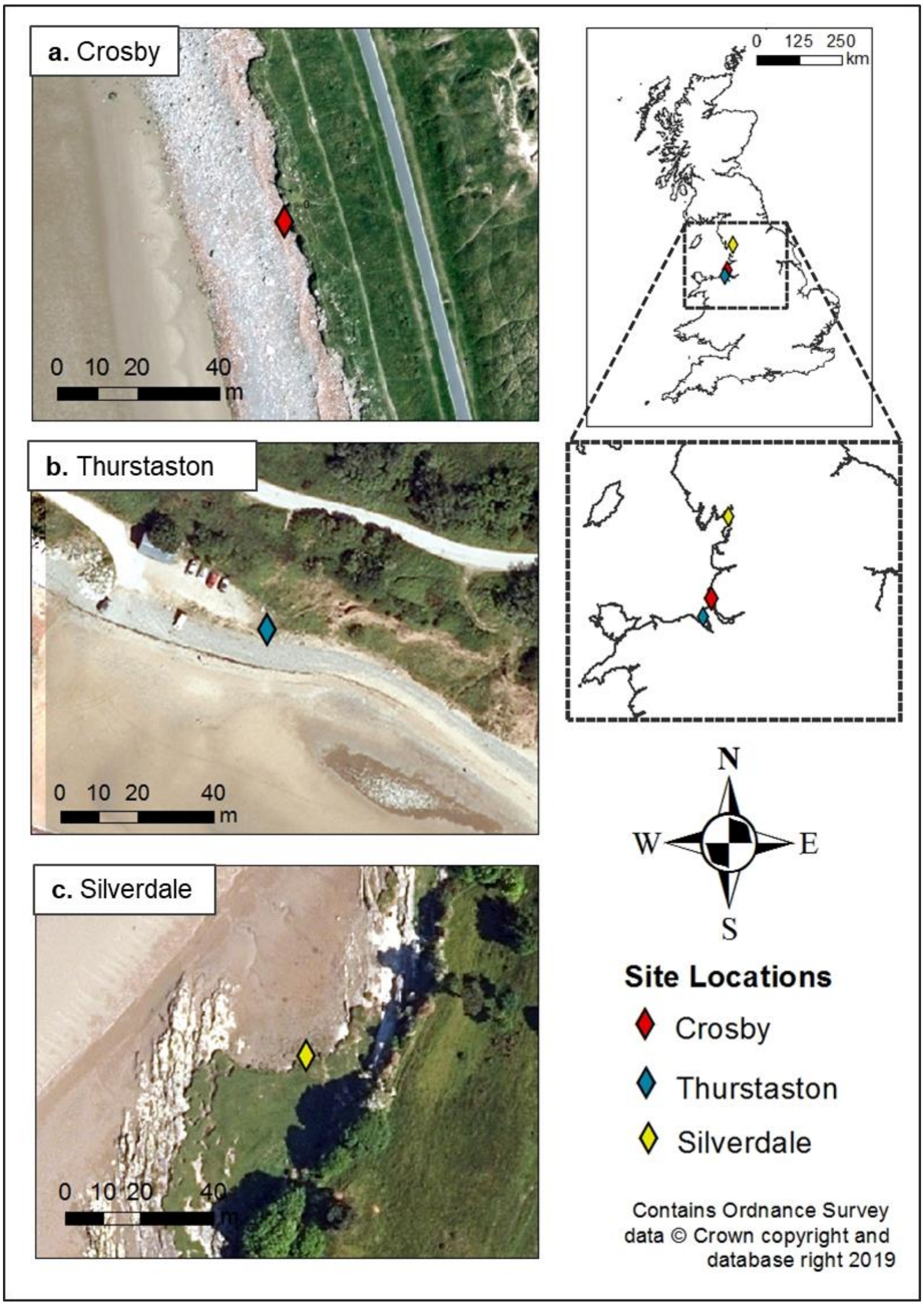

Figure 1: Locations and aerial images of Crosby (a), Thurstaston (b) and Silverdale (c) study sites.

. The average height of the cliff is ~1.5 m (vegetated on the cliff top and rubble at the base) and is classified as 'Erodible' with an expected recession of 52 m over a 20-year period (Environment Agency, 2019). Here, the objective is to reconstruct ~27 m-long site of landward retreat.

1.1.2 Thurstaston

Thurstaston is located on the west-side of the Wirral Peninsula, North West England (Figure 1b). The Dee estuary is hyper-tidal at its mouth with spring tidal range of 7-8 m

(Moore et al., 2009). Thurstaston is beach environment, and the cliffs are composed of glacial till. The coastline has experienced progressive landward retreat and recession is expected to be ~10 m over a 20-year period (Environment Agency, 2019). The study site is a low cliff formation (~1 m height) with a sloping front and an alongshore distance of ~13 m.

1.1.3 Silverdale

Silverdale saltmarsh is situated on the north-east shore of the River Kent estuary in Morecambe Bay, North West England (Figure 1c). The saltmarsh is subject to one of the largest tidal ranges in the world (10 m) and has suffered from cycles of sediment erosion and accretion that cut away at the saltmarsh edge. The coastline is considered 'Erodible' and the retreat distance calculated by the Environment Agency (2019) is ~1.7 m over a 20-year period.. The survey site is a mature, vegetated section of saltmarsh edge at ~1 m in height and a length of ~28 m.

2. Materials and Methods

A prototype camera rig, based on camera positions established in Godfrey et al. (2020), was used for systematic image acquisition. Images were processed with SfM-MVS software and the point clouds compared to TLS data through an overall 'performance' assessment.

2.1 Camera Rig Design

Optimal fixed camera positions were identified by Godfrey et al. (2020) as ≥ five images at a cliff: camera height ratio of approximately 3:4, a stand-off distance of 2 m, camera obliqueness angle of 40° declination from vertical (z-axis) and a baseline of 0.33 m & 0.22 m. Six cameras were used along a horizontal rig length of 1.65 m (approximately 97% overlap between images) and a survey pole with a maximum extension of 2.5 m (Figure 2). Images were levelled, and a remote control was used for image capture synchronisation. To maintain a consistent image overlap the camera rig was moved by a calculated distance along the cliff (D) front before capturing the images – Equation 1:

(1) $$D = 2a + b$$

where a represents the distance from the central pole to the end camera's lens (0.77 m) and b is the distance specified for the overlap of images (~0.33 m). Equation (1) gave a D value of ~1.8 m.

The camera rig was designed for a © 'GoPro Hero 4 Black' action camera. The GoPro camera has a 1/2.3 inch (6.2 x 4.65 mm) CMOS sensor. The pixel dimensions are 1.55 μm with a 4:3 aspect ratio. The GoPro has a 'fisheye' lens of 3 mm which is later corrected for in processing. The camera's angle of view (AOV) is 120° horizontally and 94° vertically when used in 'Wide' image capture mode. The GoPro is small (80 x 80 x 38 mm) and light weight (152 g) which made it useful for the multi-camera rig.

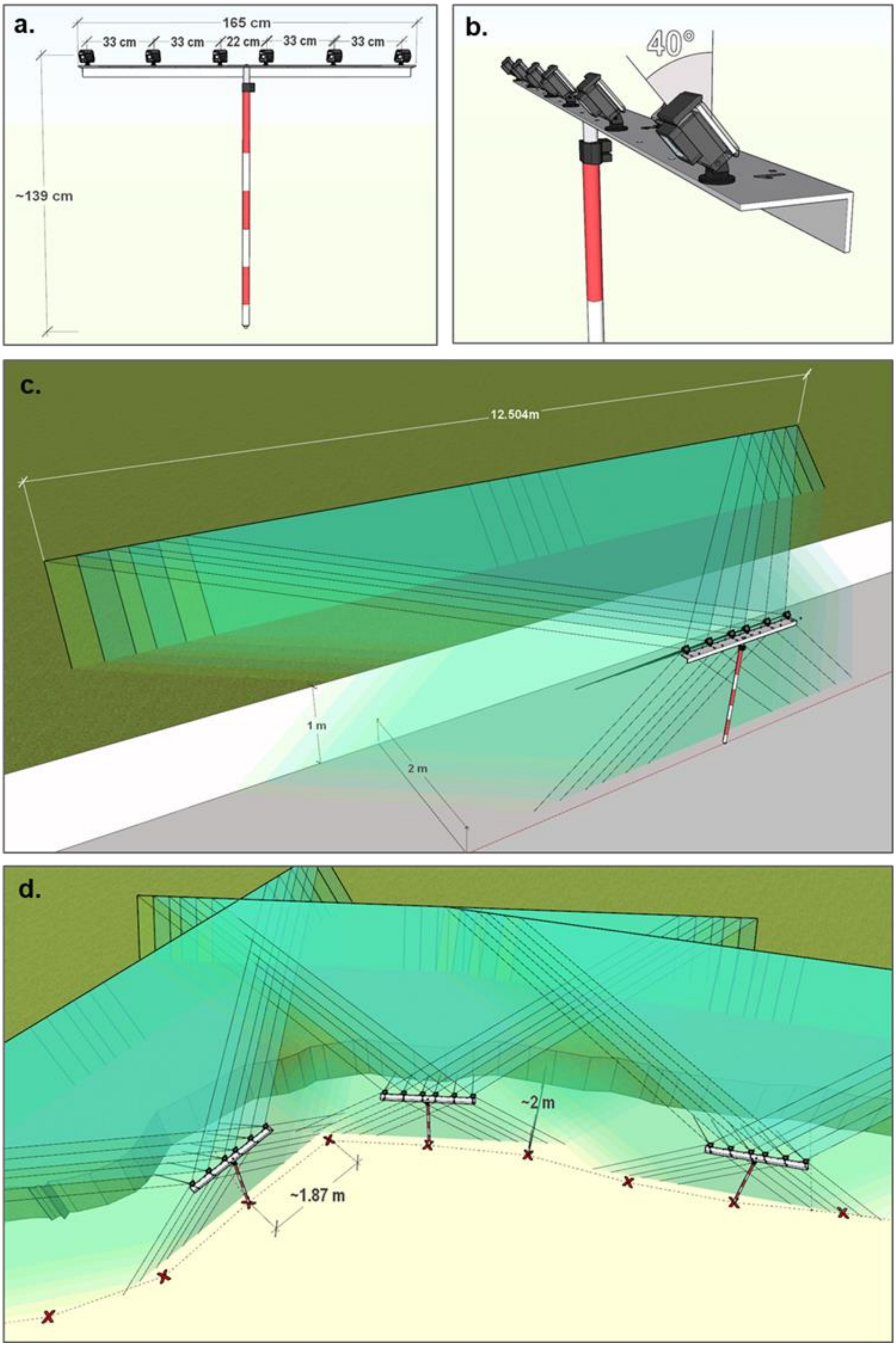

Figure 2: Camera Grid representation in SketchUp 2018. a) Camera grid dimensions showing height, width and spacing of camera. b) Camera declination from the z-axis. c) Estimated camera FOVs for the camera rig. d) Representation of camera rig movement in relation to the scene of reconstruction – the cross marks the location of the camera rig for image capture.

2.2 Data Acquisition

Thurstaston and Silverdale were surveyed in November 2018 and Crosby in December 2018. These days were chosen based on low tide and suitable weather conditions i.e. sufficient cloud cover to ensure a suitably diffuse illumination of the site (James and Robson, 2012). TLS surveys were acquired immediately after the SfM-MVS surveys, stopping at every second position of the camera rig to accommodate the TLS' scan coverage (Table 1).

The TLS survey was undertaken using a Faro 330 and scans processed in Faro SCENE 3D (v.7.1), edited to remove noise, errors and crop the areas irrelevant to the survey (Godfrey et al., 2020). The scans for each site were registered together using ground control points (GCPs) as markers for correct orientation. Average TLS mean error (mm) for each site is given in Table 1. At each site GCPs (0.15 m^2 checkerboards) were scattered across the scene approximately 1 m apart. Post SfM-MVS and TLS surveys, the checkerboards were georeferenced using a Trimble real-time kinematic global positioning system (RTK-GPS) R6 with a 8 mm horizontal accuracy and 15 mm vertical accuracy. The horizontal coordinates for the reference points were set to the British National Grid (OSTN02) while the vertical coordinates were referenced to mean sea level using the geoid model OSGM02.

The linear nature of areas of landward retreat meant image acquisition was a linear process. James and Robson (2012) discussed the increased potential of systematic distortion or 'doming' for reconstructions of this type. To reduce this potential impact, GCPs were distributed evenly across the site and continuous parallel imagery was avoided, where possible, by the inclusion of 40° vertical obliqueness and the rig positions moved relative to the orientation of the cliff face (Figure 2d).

Table 1: Data acquisition information for TLS and camera rig SfM-MVS surveys at Thurstaston, Silverdale and Crosby.

Site	Date	Images Processed	Rig stops	TLS stops	TLS Data acquisition (mins)	TLS Mean error range (mm)	SfM-MVS Image acquisition (mins)	Cliff Height (~m)	Pole Height (m)
Thurstaston	04.11.18	80	8	4	35.52	3.8	9.03	1	1.39
Silverdale	16.11.18	102	17	10	88.8	3.7	4.93	1	1.39
Crosby	04.12.18	114	19	8	71.04	7.6	6.96	1.5	2.13

3. Analysis

3.1 SfM-MVS Point Cloud Generation

SfM-MVS processing covers two main stages: first, a sparse point cloud is generated from the images; second, this point cloud is intensified through a process of densification. The aim was to optimise these two stages by speeding up processing time whilst still producing a high-quality 3D reconstruction. The process of software optimisation, therefore, entailed a two-stage assessment procedure, with the outcome of stage one processing feeding into stage two (Figure 3).

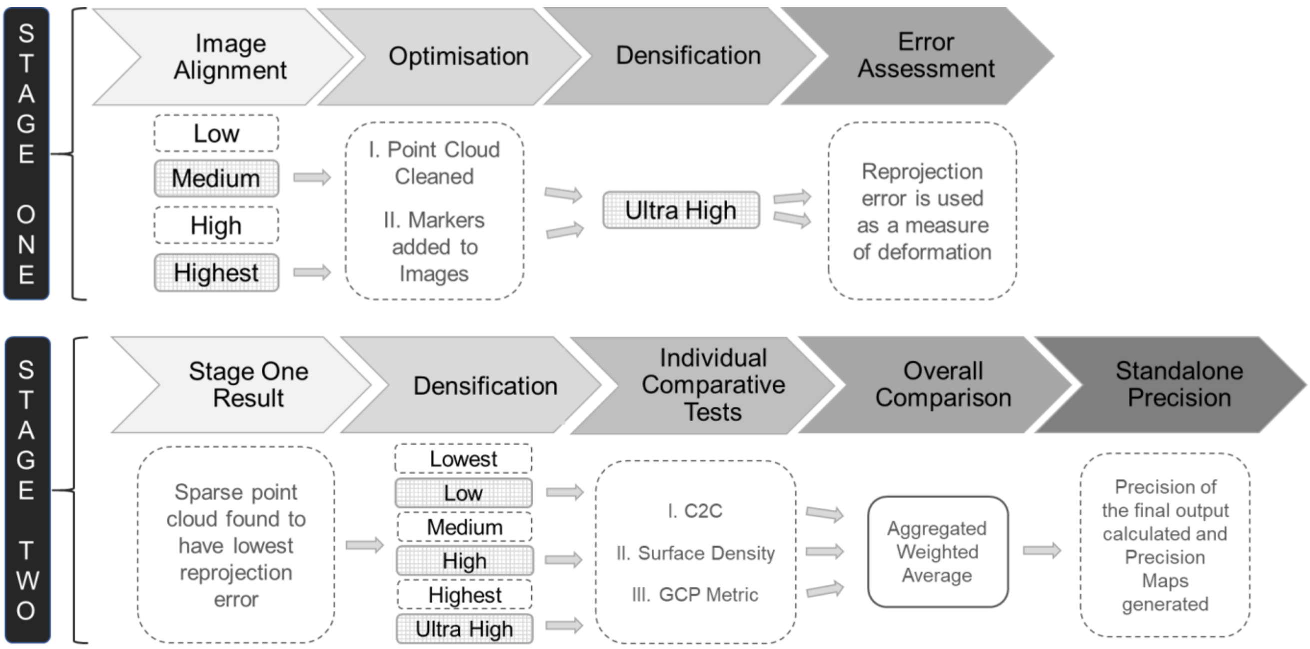

Figure 3: Workflow depicting the process of point cloud generation and assessment. Cross-hatching reflects the parameters used in processing.

Stage One processing began with the images being uploaded into Agisoft Photoscan (Version 1.3.2.42025) and the camera model being changed to 'fisheye' to match the calibration parameters of the GoPro Hero 4 Black (Godfrey et al., 2020). The process of image alignment identifies and tracks features across the uploaded images; the external and internal camera parameters are solved through a bundle adjustment and a sparse point cloud is created. The choice of image alignment parameter determines whether the image is downscaled or upscaled (software options shown in Figure 3). The alignment parameters tested in Stage One were 'Highest' (Godfrey et al., 2020) which upscales the image by a factor of 4 and 'Medium' which downscales the image by a factor of 4 (2 times by height and width of the image) (Agisoft, 2018). 'Medium' was used as a computationally faster option for larger sites. The two sparse point clouds produced were manually cleaned to remove noise and GCPs in the images referenced using software markers and the collected RTK-GPS data (section 2.2).The software markers were only placed on well-observed GCPs in the central portion of the images in order to reduce deformation brought on by the linear nature of the site and use of a fisheye lens (Figure 4a-c). The marker positions were used in the '*Optimise Cameras'* option which reduced point cloud deformation by re-running the bundle adjustment and reduces image observation error. .

The two sparse point clouds then underwent 'Ultra High' densification (Godfrey et al., 2020) to establish the impact of image alignment parameters on point cloud deformation. The subsequent reprojection error, which provides an indication of deformation, was used to determine the image alignment parameters to be used for 'Stage Two' analysis (Figure 3).

Stage Two used the findings of Stage Stage One to investigate the impact of densification through a comparison against the equivalent TLS reconstruction. The densification process intensified the number of points in the sparse point cloud and created the fundamental structure of the subsequent model. Again, there are a range of parameters within Agisoft Photoscan for reconstruction quality ranging from 'Lowest' to 'Ultra High' (Figure 3). Image downscaling underpins these parameters. The 'Ultra High' setting uses the images at their original scale and each lesser step is downscaled by a factor of 4 (Agisoft, 2018)The densification parameters chosen for testing were 'Low', 'High' and 'Ultra High' to reflect a variety of quality and timescales for a SfM-MVS reconstruction.

Figure 4: Example images used in the point cloud generation showing the estimated central placement of markers onto GCPs in Agisoft Photoscan a) Thurstaston b) Silverdale c) Crosby.

3.2 Performance Assessment

The dense point clouds produced using SfM-MVS were exported as LAZ files and their overall performance tested against the TLS benchmark. To evaluate the performance of the multi-camera rig for image acquisition and the optimal parameters within Agisoft Photoscan, a systematic method of performance assessment was undertaken using three tests. Two of the tests were previously used in Godfrey et al. (2020) and evaluated positional point accuracy (deviation analysis & GCP analysis) and the other assessed point cloud density (surface density analysis). An aggregated weighted average of the three tests was used to assess the overall performance of the camera rig image acquisition under varying densification parameters. The comparative tests are set out below:

I. Deviation analysis (B): C2C closest point distance calculation is a direct method for 3D point cloud comparison (Appendix A).

II. Surface Density Analysis (M): The surface density was estimated using CloudCompare (V2.9) which calculates the number of points present within a sphere with a specified radius (5.5 mm) (Appendix A).

III. *GCP metric* (G): This metric was used to compare the ability of the TLS and SfM-MVS to reconstruct the GCPs in the scene (Godfrey et al., 2020) (Appendix A).

Once the above three comparative tests were completed, an aggregated weighted average of SfM-MVS performance (A) was calculated for each point cloud. Point cloud deformation is a significant issue for sites with a linear image acquisition. Consequently, 50% weighting was given to the Deviation Metric (B) as it provides a clear indication of point cloud deformation and the remaining 50% was divided between GCP Analysis (25%) and Surface Density (25%) to reflect the accuracy and density of the point cloud (Equation 2):

(2) $$A = 0.50(B) + 0.25(M) + 0.25(G)$$

A score of 1 implies that SfM-MVS produced results that were (in aggregate across the three tests) of equivalent quality to those generated by the TLS.

The point clouds that provided scores most similar to the TLS for each site underwent an independent precision assessment to review the strength of the image network and influence of GCPs. The process of precision maps was developed by James, Robson and Smith (2017) and involves using Monte Carlo simulations on the bundle adjustment procedure in Agisoft Photoscan. Precision assessment is used to independently examine SfM-MVS reconstructions without a reference point cloud e.g., TLS. The precision maps produced display the spatial distribution of precision across the point cloud and represents the repeatability of the reconstruction. Greater detail on this procedure can be found in James, Robson and Smith (2017).

4. Results

4.1 Stage One Results

Stage One produced two dense point clouds for each of the three sites, one reconstructed using 'Medium' image alignment plus 'Ultra High' densification, and the second using 'Highest' image alignment plus 'Ultra High' densification. The purpose of this test was to identify the image alignment parameter that may exacerbate deformation.

All the point clouds created initially contained visible signs of deformation.As discussed in section 2.2, due to the linear nature of the site and image acquisition, reconstructions can be susceptible to the impacts of deformation, making GCPs essential. The inclusion of georeferenced data during optimisation helped to remove significant deformation by re-running the bundle adjustment with the inclusion of GCPs. This process reduced potential error on the estimated tie points and camera positions by adjusting their position to the reference coordinate system (James, Robson and Smith, 2017; Agisoft, 2018). The coordinates provided an external reference set and established an alternative method of point cloud correction without pre-processing of images.

Table 2: Reprojection Errors (m) for point clouds constructed under different Image Alignment parameters for Thurstaston, Silverdale and Crosby.

Site	Image Alignment Parameter	Densification Parameter	Reprojection Error (m)
Thurstaston	Medium	Ultra High	0.008
	Highest		0.255
Silverdale	Medium		0.012
	Highest		0.236
Crosby	Medium		0.012
	Highest		0.071

Choice of image alignment parameter revealed a further impact on point cloud deformation. Table 2 displays higher reprojection errors for all three sites when using the ‘Highest’ image alignment parameter. For example, Crosby had a reprojection error of 0.071 m (Figure 5b), in comparison the use of ‘Medium’ photo alignment produced a reprojection error of 0.012 m (Figure 5a). The reprojection error is an indicator of poor accuracy at the image alignment which can result in false matches during feature tracking. Therefore, the ‘Highest’ image alignment parameter was excluded and processing for all future reconstructions in Stage Two used the ‘Medium’ parameter.

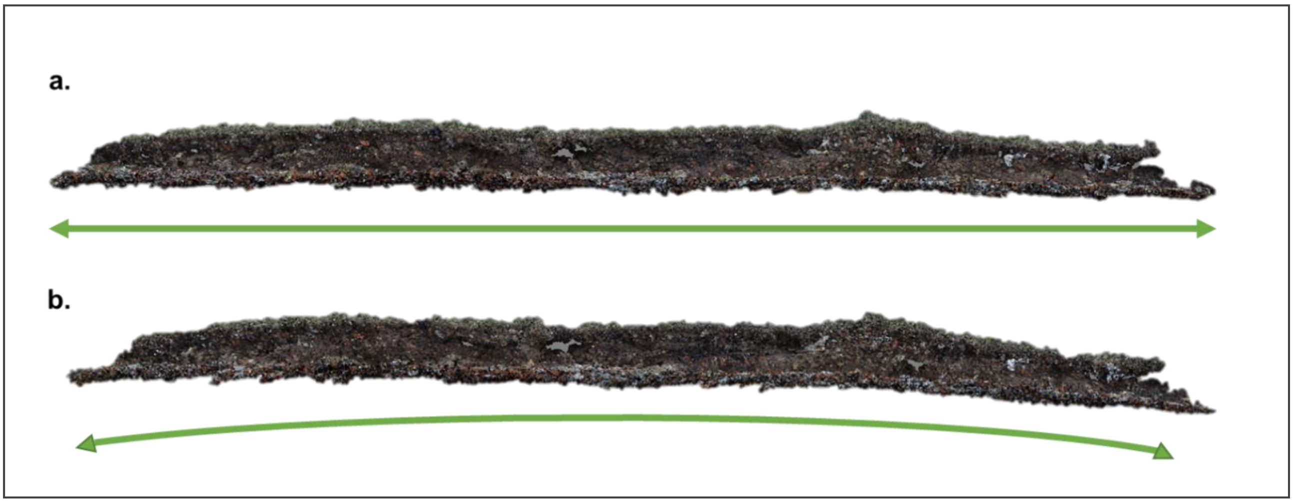

Figure 5: Crosby dense point cloud deformation under differing image alignment parameters. a) 'Medium' image alignment plus 'Ultra-High' densification. b) 'Highest' image alignment plus 'Ultra-High' densification.

4.2 **Stage Two Results**

Stage 2 results were based on point clouds created using a 'Medium' image alignment parameter, and a range of densification parameters: 'Low', 'High' and 'Ultra High' tested against a TLS benchmark.

4.2.1 Deviation Analysis Results

The mean C2C was in the range of 8-10.4 mm for all sites and densification parameters. Overall, images acquired by the camera rig displayed consistent levels of replication in comparison to the TLS dense point cloud. The TLS point cloud mean errors were between 3.7 – 7.6 mm for the three sites (Table 1). Higher deviation values were displayed for the 'Ultra High' and 'Low' densification processing parameter, with the exception of the 'Low' densification for Thurstaston. Generally, improved C2C values were created by the densification parameter 'High'.

Deviation between the SfM-MVS point cloud and the TLS are illustrated by a colour scale of difference in Figure 6 a-c. The spatial distribution of error for all sites generally followed vegetation patterns. Deviation was observed along the cliff margin at Silverdale, Crosby and in a small section of Thurstaston where vegetation was present or overhanging. There was also a minor degree of difference on the peripheries of each point cloud, all below 0.1 m difference, which was consistent with reduced image overlap. The Thurstaston reconstruction also displayed deviation in the centre of the point cloud where less features were present in the scene.

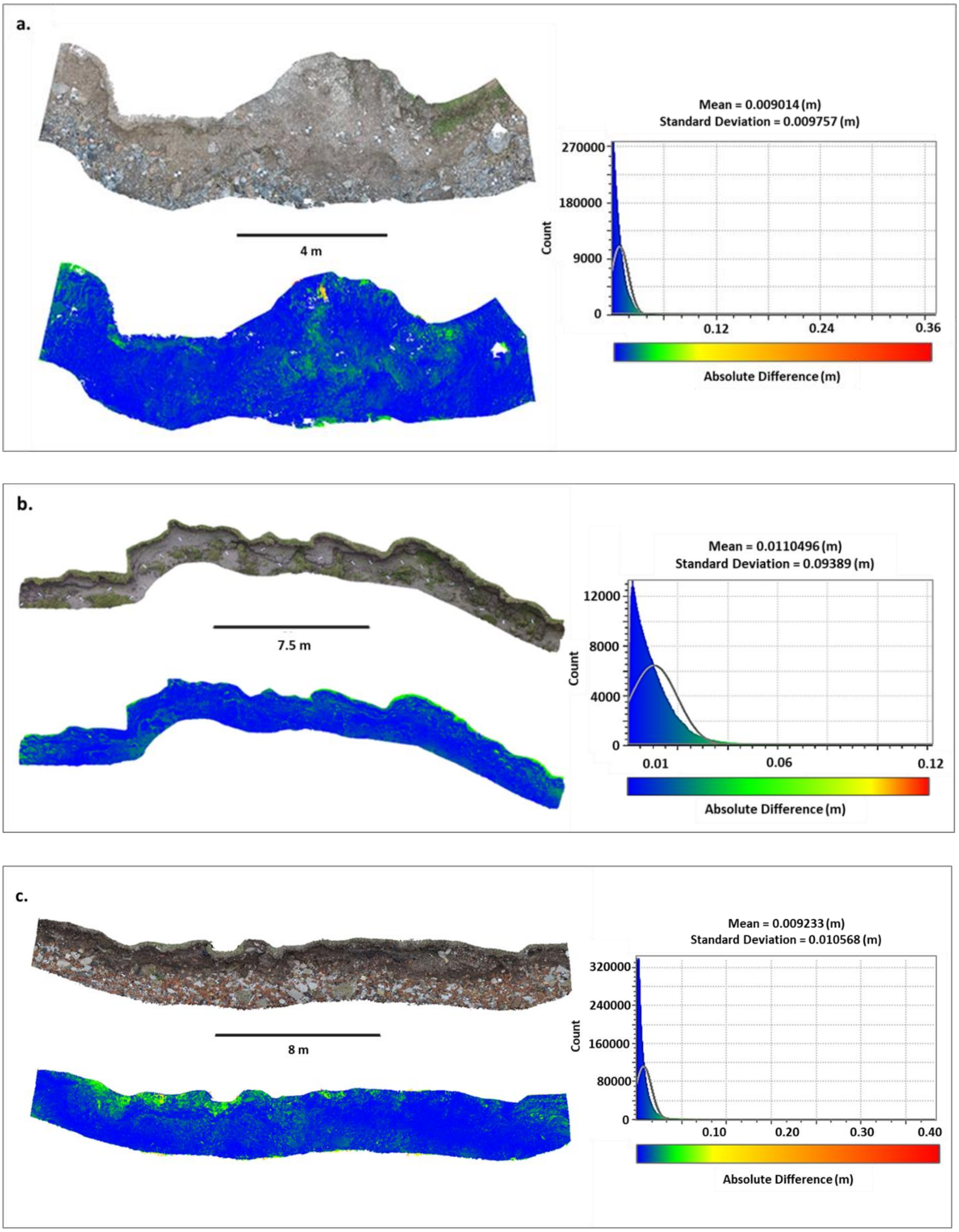

Figure 6: Scalar fields displaying the highest C2C values for each site a) Thurstaston, 'Ultra High' densification (highest mean C2C value – 9.01 mm) dense point cloud. b) Silverdale, 'Low' densification (highest mean C2C value – 10.4 mm) dense point cloud. c) Crosby, 'Ultra High' densification (highest mean C2C value 9.23 mm) dense point cloud.

4.2.2 Surface Density Results

The choice of densification parameter had an expected impact on surface density, with the 'Low' setting producing densities less than 10% of the TLS and 'Ultra High' providing the highest levels of density (Figure 7). For example, this parameter produced point clouds for Thurstaston and Silverdale that were more than twice the density of those produced by TLS. The 'High' parameter offered similar densities to the TLS.

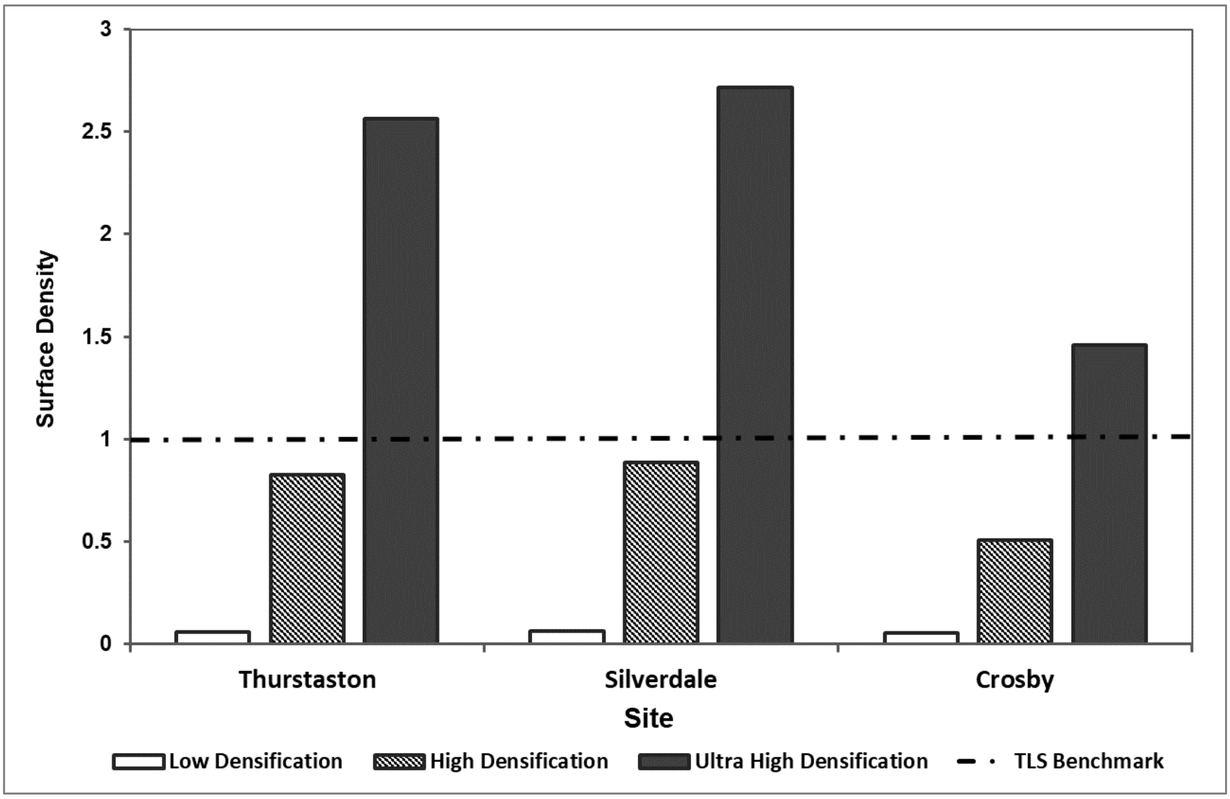

Figure 7: Surface density for each site and densification parameter compared to the equivalent TLS result.

As with the previous C2C result, vegetation had an impact on the resultant dense point cloud for both SfM-MVS and the TLS. Areas of low surface density for both techniques were those occluded by the shadowing vegetation from overhanging plants or tall plants in the foreground.

4.2.3 GCP Results

SfM-MVS produced consistently higher positional accuracy than TLS, with all results above 1 across all sites and densification parameters (Figure 8 a-c). The 'High' densification parameter provided the highest positional accuracies with an error range of 0.03 – 14.7 mm and a mean error of 1.5 mm for Thurstaston, 1.3 mm for Silverdale and 1.4 mm for Crosby. A probable cause was the 'Ultra High' densification created a degree of 'noise' within the point cloud and the 'Low' parameter did not provide sufficient points to reconstruct the dimensions of the GCP accurately.

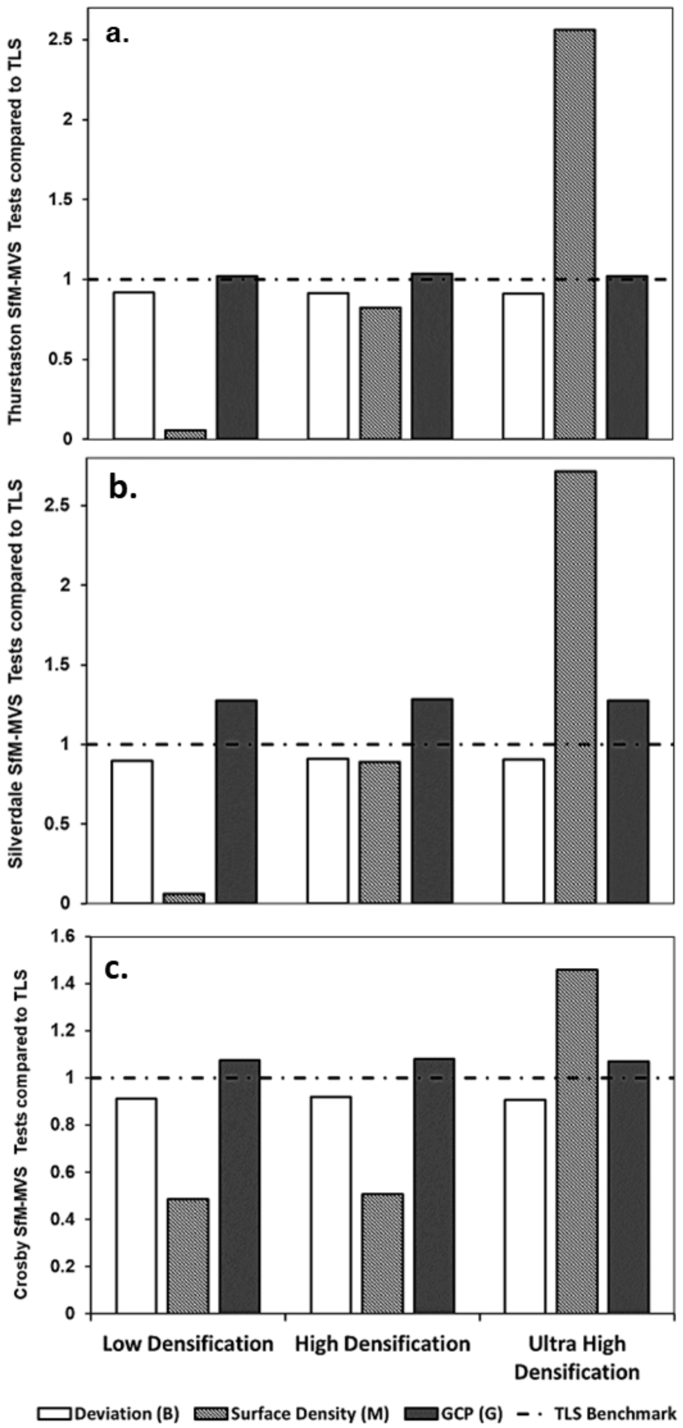

Figure 8: Results of the three comparative tests (Deviation, Surface Density, GCP) compared to the TLS reconstruction benchmark for a.) Thurstaston b.) Silverdale c.) Crosby. Reconstruction accuracies of SfM-

MVS and the TLS for each site and densification parameter. A result of 1 would imply that SfM-MVS and the TLS were equivalently accurate.

4.2.4 Aggregated Test of SfM-MVS Performance & Precision Maps

The calculation of an aggregate weighted average for the three tests provided each site and densification parameter with an overall score relative to the benchmark score of 1 for the TLS.

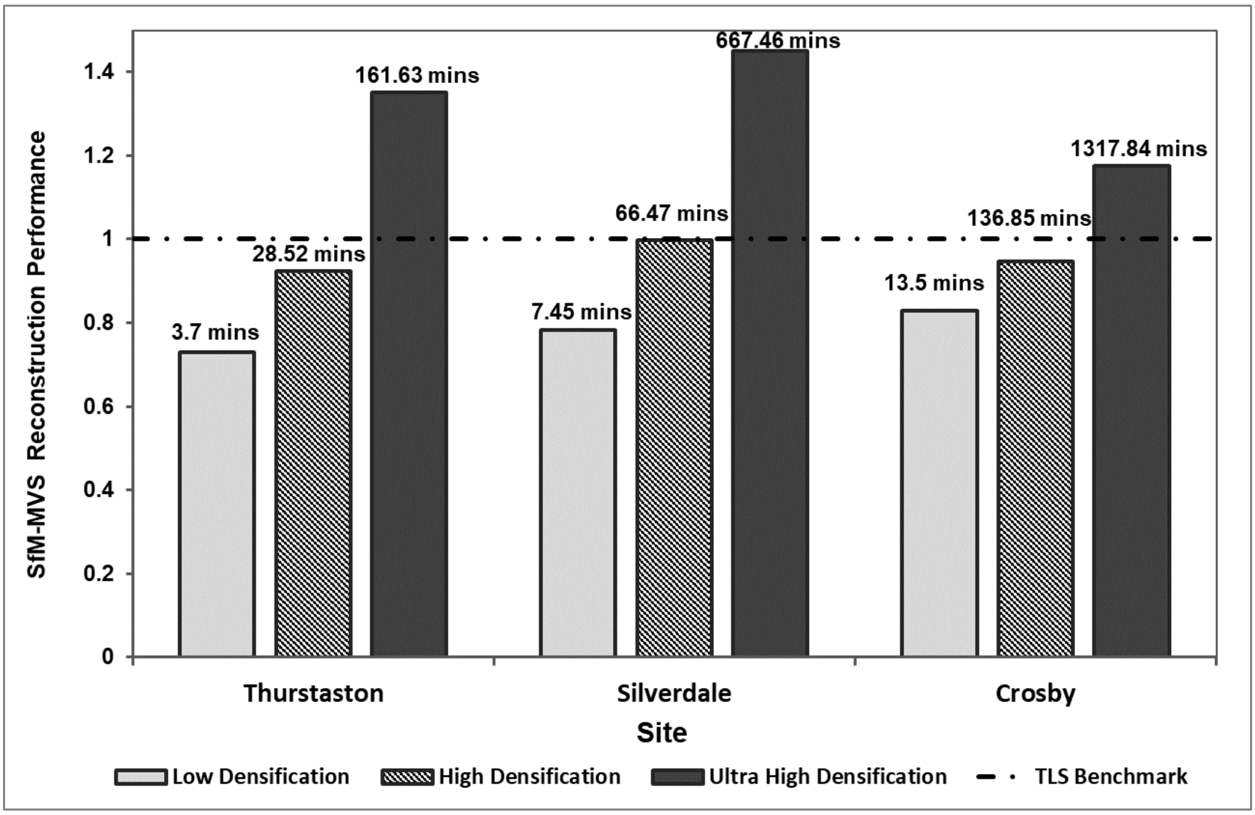

Figure 9: The overall SfM-MVS point cloud performance for each site and densification parameter compared to the TLS point cloud. The timescale for computer processing is included as a label on each column. 'Ultra High' provided the best overall score but poorest processing times.

Results show a consistent change in reconstruction performance with densification parameter across the three sites (Figure 9). 'Ultra High' produced the greatest level of performance. 'High' densification with a 'Medium' image alignment parameter provided very good replication with results reaching over 92% similarity to the TLS survey (Figure 9). An increased densification parameter had the expected impact of increasing processing time significantly (Figure 9). For example, processing took in the region of a few minutes for lower settings but took over 21 hours for the Crosby 'Ultra High' setting (Laptop: MSI GL72 7QF Intel 7 with GEFORCE GTX 960M and 16 GB RAM). Although

'High' did not reach the levels of performance provided by 'Ultra High' densification, it offered a result within >92 % similarity of the TLS with 87% less processing time on average. As a result of these lower processing times and high similarity with the TLS, point clouds created through a 'Medium' image alignment and 'High' densification were used to assess precision (Figures 10-12).

The precision maps allowed the spatial distribution of precision to be visualised and the separate influences of image network geometry (internal precision) and GCPs (external precision) to be understood (James, Robson and Smith, 2017) - blue referring to increased precision.

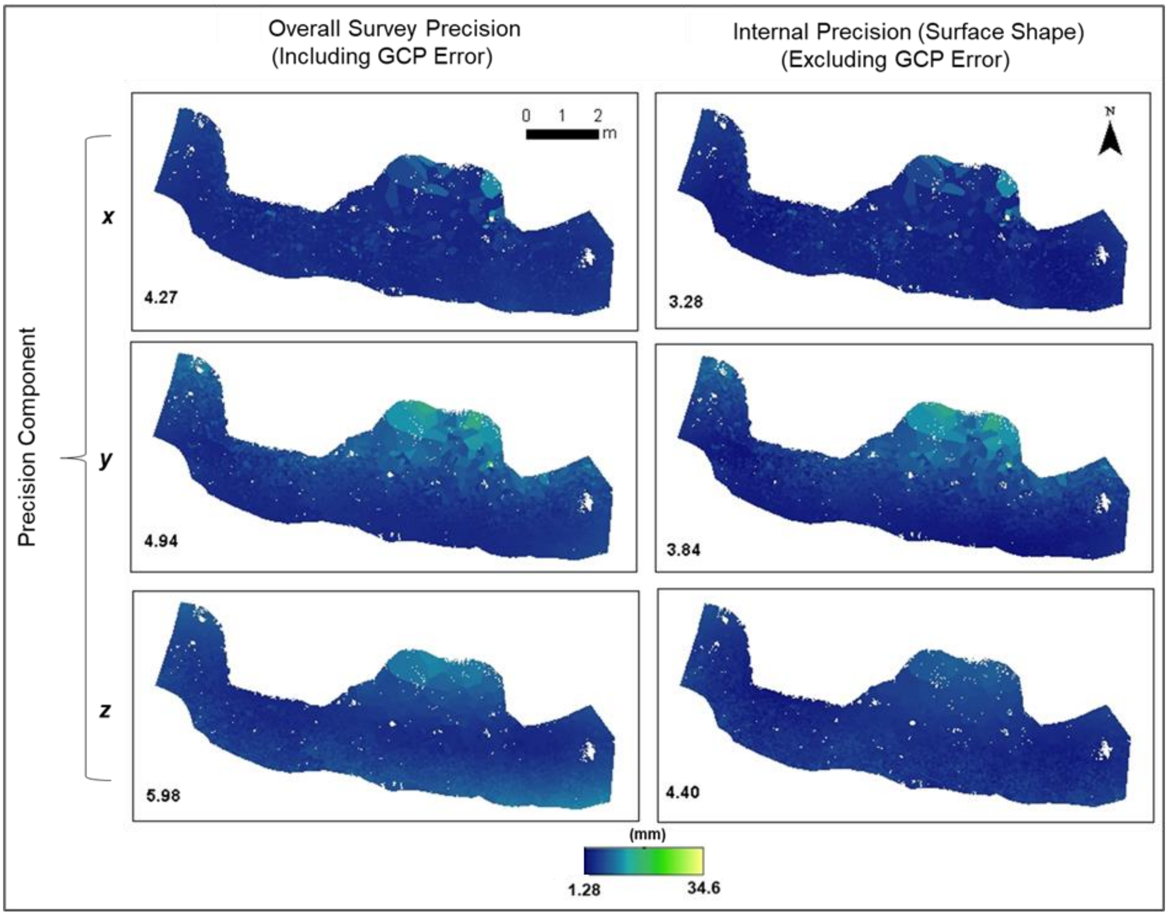

Figure 10: Precision error maps separated into x, y and z components for Thurstaston. Overall survey precision including georeferencing error and internal precision (surface shape error) excluding any georeferencing error are displayed in two columns. Mean precision (mm) is displayed on the bottom left of each map.

The Thurstaston reconstruction showed millimetre mean precision across all three dimensions, with all dimensions (*x, y* and *z*) providing values < 6 mm (Figure 10).

Precision estimates displayed a slight offset, approximately 1 mm, between internal (Shape) and external (Overall) precision. The lower internal precisions (Figure 10) suggest the image acquisition scheme provided a strong image network, producing robust feature tracking and tie points.

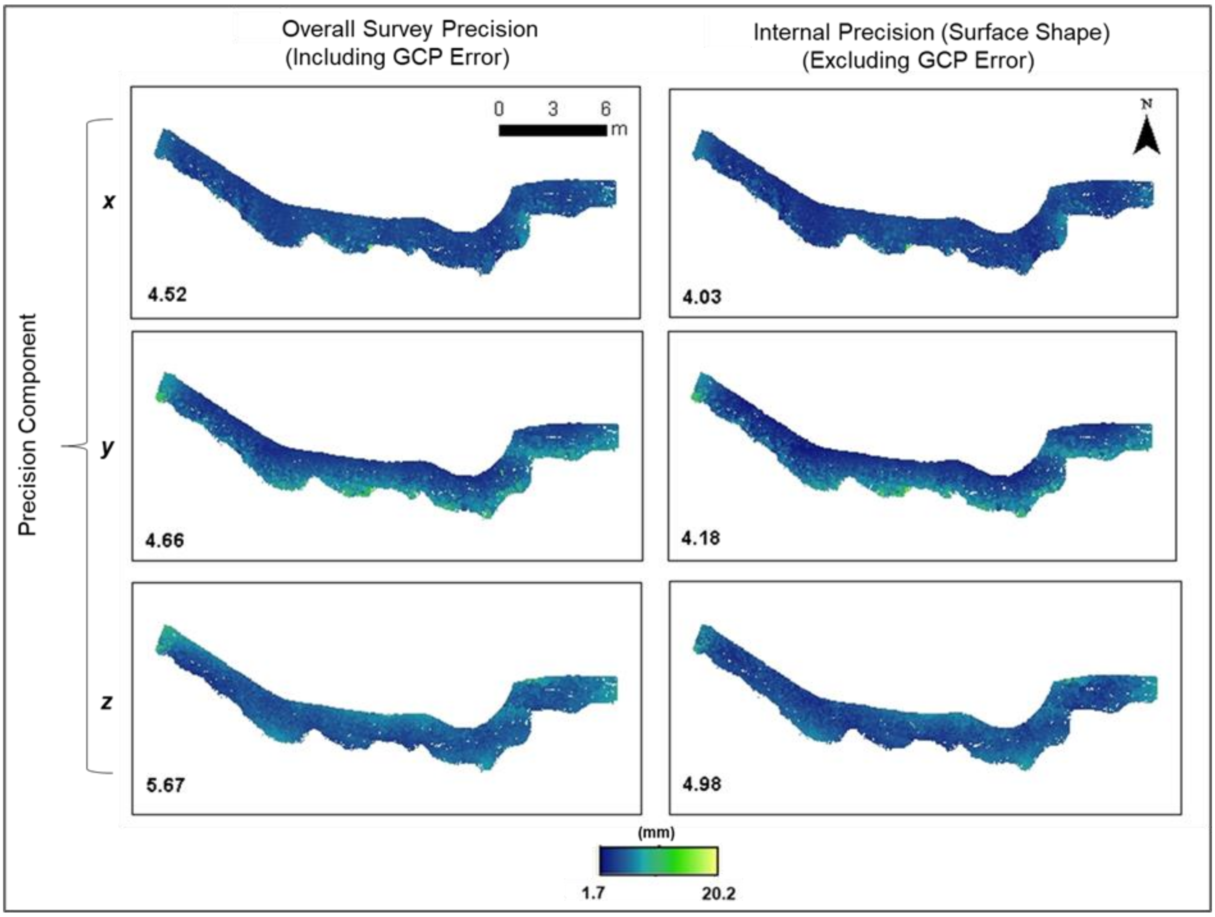

Figure 11: Precision error maps separated into x, y and z dimensions for Silverdale. Overall survey precision including georeferencing error and internal precision (surface shape error) excluding any georeferencing error are displayed in two columns. Mean precision (mm) is displayed on the bottom left of each map.

Precision maps for Silverdale also showed millimetre mean precision for each dimension for both internal and external precision – all less than 6 mm (Figure 11). Overall, the reconstruction had slightly higher precision values than Thurstaston but only a very minor offset between external and internal precision, suggesting strength in both the image and GCP network.

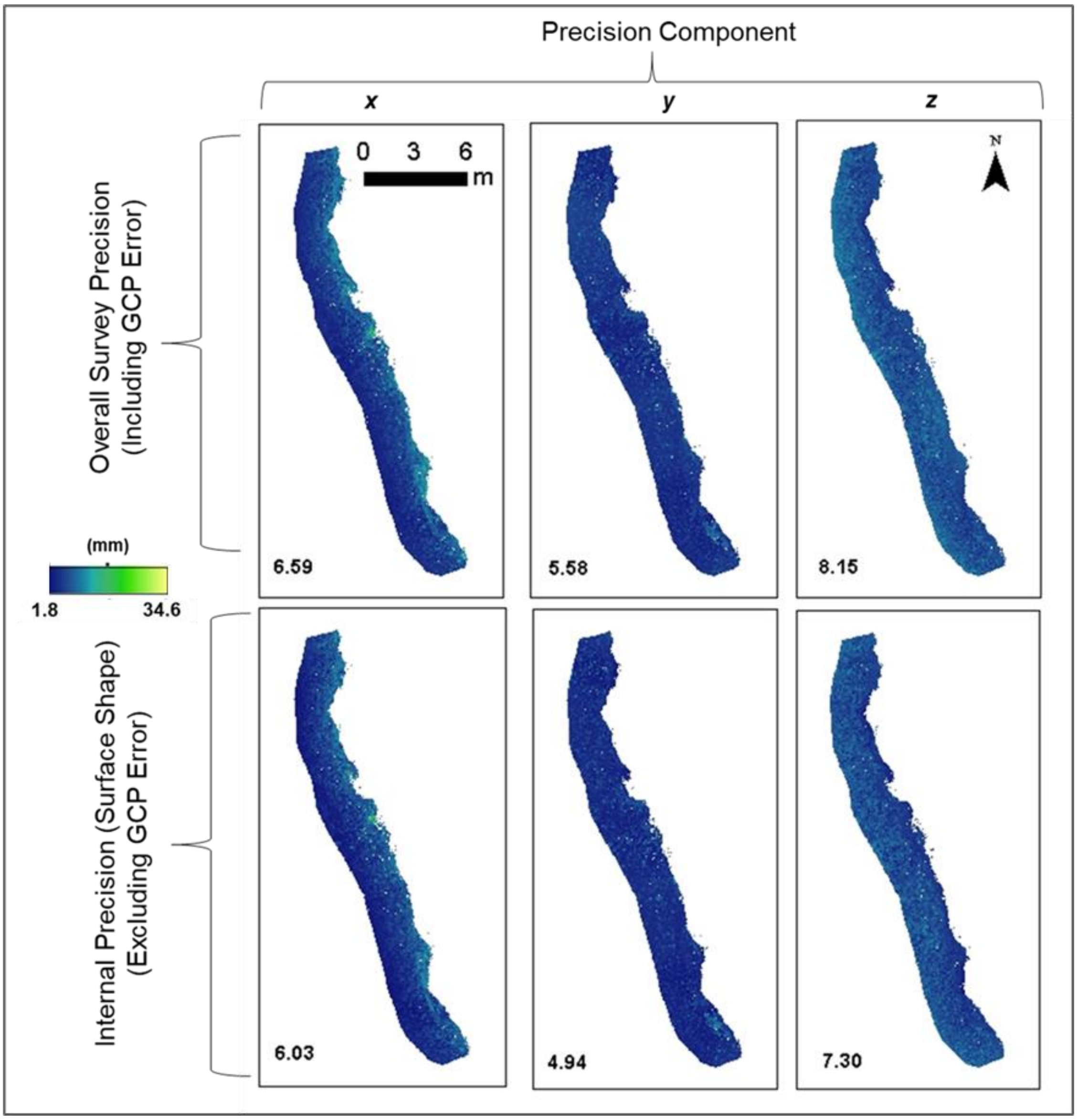

Figure 12: Precision error maps separated into x, y and z dimensions for Crosby. Overall survey precision including georeferencing error and internal precision (surface shape error) excluding any georeferencing error are displayed in two rows. Mean precision (mm) is displayed on the bottom left of each map.

The Crosby reconstruction showed millimetre precision for each dimension (Figure 12). Precision estimates for both overall precision and shape values lied close together but with an offset of approximately 1 mm in each plane. However, the scale and similarity of magnitude in overall and shape precision suggested both good image network geometry and GCP distribution and measurement. The scale and spatial distribution of estimated precision both internally and externally corresponded with the C2C results (combined *x, y* and *z*) in section 4.2.1. Poorer precision estimates were present along the cliff where vegetation is present.

5. Discussion

Images obtained using the camera rig produced point clouds with reconstruction quality similar to, and indeed exceeding, a TLS. The systematic approach to image acquisition and processing with SfM-MVS provided consistent reconstruction results across all three sites. Thus, the findings provide a valuable first step in the use of multi-camera setups and offers new understanding that will benefit projects which look to use more robust camera types or alternative camera setups for rapid and low cost assessment of coastal recession.

5.1 Reconstruction Comparison

The use of the camera rig with SfM-MVS displayed an average error of 8.93 mm deviation from the TLS across all three sites and densification parameters. In this study, as with Castillo et al. (2012), Nouwakpo et al. (2016) and Westoby et al. (2018), the TLS is the assumed benchmark standard for comparison of image-based 3D reconstruction. However, error is inherent within all monitoring techniques including TLS. The TLS surveys produced average errors in the range of 3.7 mm to 7.6 mm (Table 1). Consequently, when comparing the SfM-MVS point cloud to the TLS, the measured deviation may appear inflated when it reflects some of the error present within the reference survey.

The standard deviation of distance between point clouds has been used as an indicator for reconstruction quality by Nouwakpo et al. (2016) whose work will be used as comparator (Table 3). The average standard deviation across all three sites using 'Medium' alignment and 'High' densification compared to the TLS was 7.8 mm. Nouwakpo et al. (2016) recorded standard deviation values of 5 mm over a 6 m plot when comparing a TLS and pole-mounted SfM-MVS image acquisition (DSLR). The standard deviation results display a similar order of magnitude, with an offset of 2.8 mm, on average. However, the scale of sites in this current paper is more than double that of Nouwakpo et al. (2016). A standard deviation measure relative to length of site offers the opportunity for improved context of these results (Table 3).

Table 3: Calculation of dimensionless indictor based on standard deviation from the three study sites compared with data from Nouwakpo et al. (2016).

	Mean Standard Deviation (mm)	**Length of Site (m)**	**Dimensionless Indicator**
Thurstaston	7.5	13	0.58
Silverdale	8	28	0.29
Crosby	7	30	0.23
Nouwakpo et al. (2016)	5	6	0.83

Nouwakpo et al. (2016) report reconstruction quality poorer than all three sites surveyed with the camera rig (Table 3). The greatest difference from the findings of Nouwakpo et al. (2016) were the results of the Crosby survey, where there was a 72 % improvement in the standard deviation relative to the length of site. Although there is a need for greater research into the impact of stand-off distance and site complexity, these results provide encouraging findings for systematic image acquisition using multiple cameras.

Independent precision estimates for all sites showed millimetre-scale results. The inclusion of independent precision estimates helped to provide a holistic view of reconstruction quality. Precision estimates (both internal and external) for the three sites ranged from 3.28 mm – 8.15 mm (*x, y* and *z*). Internal precision displayed marginally lower values than external values, suggesting a minor propagation of error produced from the measurement of the GCPs. The reduced precision in the z-axis across all three sites is consistent with reduced vertical accuracy (~15 mm) of the RTK-GPS relative to horizontal accuracy (~8 mm). James et al. (2017) reported a much greater offset of 40 mm between internal and external precision for simulated UAV flights. The scale and distribution of precision across the three surveyed sites was consistent, and in line with the spatial distribution of error produced in the C2C analysis. The variation in precision between sites reached a maximum of 3 mm. All sites have shown ≤ 8.15 mm precision estimates in each dimension, suggesting a good image network through the use of oblique and well captured images that produced high quality tie points. Minor offsets between internal and external precision were present at all sites suggesting a good distribution of GCPs and good image network geometry. Crosby shows slightly poorer precision values than Thurstaston and Silverdale. This difference may be the consequence of increased linearity of the site, reducing the possibility of more convergent images and reducing the quality of the reconstruction. Crosby and Thurstaston show a marginally higher but similar magnitude offset between internal and external precision (~1 mm) suggesting that the minor errors present in the GCP measurement propagated through the reconstruction to produce a slightly poorer external precision value.

5.2 Influence of Processing and GCPs

The influence of image processing proved to be a significant contributor to the overall reconstruction quality when using a systematic approach to SfM-MVS.

5.2.1 GCP Influence

The three sites surveyed provided good texture for feature extraction, but the thin linear geometry of the site meant a potential for a 'drift' in the estimation of internal and external camera parameters (James and Robson, 2012). Drift can lead to systematic deformation and may be more prevalent in action cameras due to the increased lens distortion. The inclusion of GCPs in the field is necessary to reduce deformation at sites with a linear image acquisition (James and Robson, 2012) and an increase in the number of GCPs has shown to improve survey accuracy (Warrick et al., 2017; Westoby et al., 2018). Precision estimates across all sites showed good GCP networks with precision similar in scale to the image network estimates (all sites < 8.2 mm precision for *x, y* and *z*). The minor offset of internal and external (~ 1 mm) precision shows the GCP network has improved (distribution and number) since Godfrey et al. (2020), in which the external precision estimate revealed a greater offset between internal and external precision (offset of ~ 7 mm on average across *x, y* and *z*).. Although precision estimates suggested a good image network geometry, the estimates did not consider the potential for systematic deformation. This form of deformation was more easily identified through the reprojection error and, subsequently, removed during stage one processing through strategic marker placement and choice of processing parameter (section 4.1).

5.2.2 Influence of Processing Parameters

The choice of processing parameter also proved to be influential on overall point cloud reconstruction. The choice of Stage One image alignment parameter showed considerable impact on systematic deformation with the 'poorer' image alignment setting ('Medium') providing a reconstruction that had 18 times, on average, less reprojection error (an initial indicator for systematic deformation) than the 'Highest' setting. The 'Highest' image alignment parameter upscaled the image by a factor of four and, therefore, introduced an increased number of feature matches across distorted portions of the image.

The quality of reconstructions from overlapping 2D images is known to be significantly dependent on image content and subsequent feature matching (Gruen, 2012). Therefore, cameras with greater FOVs, such as action cameras provide a high degree of feature tracking (Streckel & Koch, 2005). Thus the combination of a linear image capture and a wider FOV encouraged feature tracking across the distorted borders of the image, impairing the software's ability to adequately estimate camera pose, image network geometry and, therefore, reconstruction quality (James and Robson, 2012; Eltner et al., 2016). Although the poorer reprojection error provided by the 'Highest' image alignment parameter may appear contradictory, the upscaling of the image encouraged matches with poor covariance and thus a poor estimation of camera pose and orientation. Consequently, the downscaling of the image ('Medium' image alignment parameter) 'forced' the software to use larger, more stable features as keypoints and so there was a lower likelihood of systematic error through 'drift' in camera pose estimation. Similar conclusions were also made by Prosdocimi et al. (2015), who documented how decreasing image resolution (e.g. downscaling) led to reduced error potentially due to error smoothing.

The choice of densification parameter (Stage Two) had a marked impact on SfM-MVS performance. The densification process improved the reconstruction with each higher interval. Here, densification multiplied the tie points established in the image alignment stage and did not optimise any aspects of the point cloud, making it a less influential step (James, Robson and Smith, 2017). The choice of densification parameter i.e., medium, high, ultra-high can produce a result that under performs, equals, or surpasses the point density of the TLS reconstructions. Eltner & Schneider (2015) and Smith and

Vericat (2015) also found SfM-MVS to outperform the TLS on small-scale sites with single cameras.

The ‘Ultra High’ densification parameter required longer processing times than the ‘High’ setting (increase of 87% on average), potentially increasing density without substantial advantage. Extended processing time during the densification stage is not uncommon in SfM-MVS research, particularly when using large datasets (Nagle-McNaughton & Cox, 2020). However, the results reported in this paper found that the ‘High’ densification parameter offered in Agisoft produced results only 4.39 % dissimilar to the TLS on average across all three sites and processing of approximately $1/8^{th}$ of the time, on average. This represented a significant gain in efficiency, important where processing power is limited, time is constrained, or the image dataset is large.

5.3 **Future Research**

Overall, the multi-camera rig provides a rapid, systematic and accurate method of image acquisition for SfM-MVS. Across all sites the 3D reconstructions from the rig have shown consistently strong results in comparison to the TLS and through independent precision assessment. The choice of a nominally lower image alignment parameter, ‘Medium’, provided decreased reprojection error and less deformation. The combination of ‘Medium’ image alignment with the ‘High’ densification setting provided results that were >92 % similar to TLS. The benefit of using a lower image alignment parameter does not mean the choice of the ‘Highest’ parameter may not be advantageous for other reconstructions, as deformation may be less prevalent at sites where a 360° image capture is possible. This research corroborates the suggestions of Brasington, Vericat and Rychkov (2012) and Eltner et al. (2016) that diligent selection of processing parameters post-image acquisition is an important step for optimising reconstruction quality.

Data acquisition using the rig also proved to be considerably faster than using a TLS. The camera rig provided a data acquisition 10.71 times faster, on average, than the TLS across the three sites. This reduction in time is particularly important with respect to fieldwork in marine and coastal settings where tides and weather can reduce the accessibility of sites and rapid acquisition of field data can be vital to fully survey an area.

The findings reveal the camera rig is a low cost (~£600) and resource efficient alternative to the TLS (~£35,000; Visser et al., 2019), producing reconstructions that are similar to, and in some cases even exceed, the TLS benchmark. The strong precision values established for all sites revealed that the camera rig, in combination with the placement of the GCPs produced a strong image network geometry and robust GCP network. Thus, this new form of data acquisition provides a systematic, easily followed process that secures a level of coverage that may not be as achievable for less experienced users of SfM-MVS.

Future work should consider:

a) The setup of the multi-camera rig was specifically designed for sites of coastal recession of a particular height range and a specified stand-off distance. Exploring the use of multi-camera setups in different environment settings and scales would expand the potential of the multiple cameras.

b) Software marker placement displayed an influence on reconstruction. A focussed examination of the impact of software marker placement on 3D reconstruction quality would interesting, particularly, the impact on different lens types e.g., DSLR compared to fish-eye.

c) Further research could explore adaptions to the multi-camera rig such *as in-situ* monitoring with permanent camera positions.

d) Comparisons with other SfM-MVS image acquisition schemes such as single DSLRs or other platforms could provide further details on the accuracy and usability of multi-camera setups.

e) The combination of multiple cameras and a GNSS system in a single unit may provide the opportunity to remove GCPs and further reduce surveying time.

f) The stand-off distance for the camera rig was set to 2 m to ensure observed changes were not the result of alternating image resolution (James and Robson, 2012). However, the impact of changing distance on accuracy and precision values could be explored in future research.

6. Conclusions

The rig provided a systematic and effective method of image acquisition that proved to be ~11 times faster than the TLS, on average, across the three test sites. Comparative tests with a TLS showed overall reconstruction quality that could equal (> 92 % similarity) or surpass the TLS benchmark depending upon selected processing parameters. The image alignment parameter proved to significantly influence point cloud deformation at all three test locations with an average reduction of 94 % in reprojection error through a change in processing parameter ('Medium' instead of 'Highest'). The choice of densification parameter had a significant bearing on processing times with 'Ultra High' parameter increasing times by 87% on average. However, a marginally lower densification parameter ('High') offered results only 4.39 % dissimilar from the TLS and processing of approximately $1/8^{th}$ of the time on average.

Independent precision estimates across all three test locations were < 8.2 mm for *x, y* and *z* dimensions, suggesting consistent levels of reconstruction across varying alongshore scales. The research has revealed increased speed of data acquisition in comparison to a TLS, as well as the simplified nature of the image capture network, allowing images to be acquired systematically for sites of coastal recession.

This research provides several advancements in terms of the practical application of SfM-MVS in the field. The camera rig offers an affordable, accurate, easily operable and rapid option for monitoring coastal recession without regulatory restriction. These practical implications of the work are important in supporting the real-world implementation of the coastal monitoring techniques for practitioners and policy makers that may not have large budgets or specialist expertise available to them.

For SfM-MVS researchers, the paper takes some of the first steps into the use of roving multiple cameras. The evidence on the successful use of action cameras, alternative processing options for reducing deformation and computational processing times illustrates exciting avenues for further research.

Figures & Table Captions

Figures:

Figure 1: Locations and aerial images of Crosby (a), Thurstaston (b) and Silverdale (c) study sites.

Figure 2: Camera Grid representation in SketchUp 2018. a) Camera grid dimensions showing height, width and spacing of camera. b) Camera declination from the z-axis. c) Estimated camera FOVs for the camera rig. d) Representation of camera rig movement in relation to the scene of reconstruction – the cross marks the location of the camera rig for image capture.

Figure 3: Workflow depicting the process of point cloud generation and assessment. Cross-hatching reflects the parameters used in processing.

Figure 4: Example images used in the point cloud generation showing the estimated central placement of markers onto GCPs in Agisoft Photoscan a) Thurstaston b) Silverdale c) Crosby.

Figure 5: Crosby dense point cloud deformation under differing image alignment parameters. a) 'Medium' image alignment plus 'Ultra-High' densification. b) 'Highest' image alignment plus 'Ultra-High' densification.

Figure 6: Scalar fields displaying the highest C2C values for each site a) Thurstaston, 'Ultra High' densification (highest mean C2C value – 9.01 mm) dense point cloud. b) Silverdale, 'Low' densification (highest mean C2C value – 10.4 mm) dense point cloud. c) Crosby, 'Ultra High' densification (highest mean C2C value 9.23 mm) dense point cloud.

Figure 7: Surface density for each site and densification parameter compared to the equivalent TLS result.

Figure 8: Results of the three comparative tests (Deviation, Surface Density, GCP) compared to the TLS reconstruction benchmark for a.) Thurstaston b.) Silverdale c.) Crosby. Reconstruction accuracies of SfM-MVS and the TLS for each site and densification parameter. A result of 1 would imply that SfM-MVS and the TLS were equivalently accurate.

Figure 9: The overall SfM-MVS point cloud performance for each site and densification parameter compared to the TLS point cloud. The timescale for computer processing is included as a label on each column. 'Ultra High' provided the best overall score but poorest processing times.

Figure 10: Precision error maps separated into x, y and z components for Thurstaston. Overall survey precision including georeferencing error and internal precision (surface shape error) excluding any georeferencing error are displayed in two columns. Mean precision (mm) is displayed on the bottom left of each map.

Figure 11: Precision error maps separated into x, y and z dimensions for Silverdale. Overall survey precision including georeferencing error and internal precision (surface shape error) excluding any georeferencing error are displayed in two columns. Mean precision (mm) is displayed on the bottom left of each map.

Figure 12: Precision error maps separated into x, y and z dimensions for Crosby. Overall survey precision including georeferencing error and internal precision (surface shape error) excluding any georeferencing error are displayed in two rows. Mean precision (mm) is displayed on the bottom left of each map.

Tables:

Table 1: Data acquisition information for TLS and camera rig SfM-MVS surveys at Thurstaston, Silverdale and Crosby.

Table 2: Reprojection Errors (m) for point clouds constructed under different Image Alignment parameters for Thurstaston, Silverdale and Crosby.

Table 3: Calculation of dimensionless indictor based on standard deviation from the three study sites compared with data from Nouwakpo et al. (2016).

Supplementary Material

Appendix A - Comparative Testing Details

I. Deviation analysis (B): The details of this test are provided in Godfrey et al., 2020 but will be provided here again for clarity. C2C closest point distance calculation is a direct method for 3D point cloud comparison and was used in Godfrey et al., 2020. "*The C2C test calculated the mean distance (combined x, y and z) and standard deviation in distance across each point cloud. A scalar field was then generated which was coloured to represent areas of greater deviation. The resulting mean C2C distance (j) was expressed relative to a 100 mm scale in the form of a deviation metric (B) – Equation 3. The deviation metric (B) was then used in the overall performance assessment against the TLS (Equation 8).*"

(3) $$B = \lim_{j \to 100} 1 - \left(\frac{j}{100}\right)$$

I. Surface Density Analysis (M): The estimation of point cloud density is an important step to judge the coverage of the 3D reconstruction. The surface density was estimated using CloudCompare (V2.9) which calculates the number of points present within a sphere with a specified radius (5.5 mm). The sphere is aligned with each point in the point cloud and the number of surrounding points estimated. The result is the mean density, standard deviation in density and a scalar field which represents areas with higher or lower surface density. This process was also undertaken for the TLS point cloud as a benchmark for comparison and offers a method for comparing the level of coverage of the point cloud. Equation 4 was used to compare the surface density for SfM-MVS (R_s) relative to the TLS surface density (R_t). The surface density metric (M) was then used in the overall performance assessment (Equation 2)

(4) $$M = \frac{Rs}{Rt}$$

I. *GCP metric (G)*: This metric was used to compare the ability of the TLS and SfM-MVS to reconstruct the GCPs in the scene. The details of this test are provided in Godfrey et al., 2020 but will be provided here again for clarity. "*Expressions (5) and (6) describe the test of accuracy for both TLS and SfM-MVS (P_S refers to the accuracy of SfM, P_t refers to the performance of the TLS). Firstly, under- and over-measurement of the GCPs had to be treated equitably. The conditional statement ('if, then' denoted by the logical operator →) occupying the numerator space in equations (5) and (6) describes this process (S represents SfM-MVS and T represents TLS measured values).*

Following the logical process, the value was then divided by the GCP known value (R) to obtain a ratio of each method of reconstruction's error relative to reality. Subtracting this result from 1 provided a measure of how accurate the method of reconstruction had been at recreating the known dimensions of the GCP.

(5) $$P_S = 1\text{-}\left\{\frac{[(S>R)\rightarrow(S-R)]\vee[(S<R)\rightarrow(R-S)]}{R}\right\}$$

(6) $$P_t = 1\text{-}\left\{\frac{[(T>R)\rightarrow(T-R)]\vee[(T<R)\rightarrow(R-T)]}{R}\right\}$$

(7) $$Q = \frac{P_S}{P_t}$$

Equation (7) describes the ratio of the results of equations 5 and 6 and compares the ability of SfM-MVS to accurately reconstruct the GCP compared to the TLS. If SfM-MVS proved more accurate than the TLS a value for Q of >1 would be returned for each of the GCPs. This test was applied to the x (alongshore) and y (cross-shore) axes of the GCPs at each site. There was a varying number of GCPs at each location, therefore, Equation 8 was used to accommodate the varying number of GCPs: i represented the varying number of

GCP measurements (x & y) and was equal to 18 at Thurstaston, 50 at Silverdale and 42 at Crosby:

$$(8) \quad G = \sum_{i=1}^{n} \frac{1}{i} (Q_i)$$

The Q value for each of the GCP measured in the point cloud was weighted by 1/i to reflect the number of GCP used in the metric. These calculations were only performed for GCPs at the base of the cliff were there was no impact from vegetation. If one of the techniques was able to reconstruct a GCP while the other was unable, the former was given a value of 2 in order to reflect the ability of one monitoring techniques ability to reconstruct a GCP over the other."

Acknowledgements & Funding

This research was supported through the European Regional Development Fund (22R15P00045) Low Carbon Eco-innovatory with industrial partner Marlan Maritime Technologies Ltd.

Author Contributions

Conceptualization: Samantha Godfrey, Andrew Plater.

Methodology: Samantha Godfrey, James Cooper, Andrew Plater

Validation: Samantha Godfrey

Formal Analysis: Samantha Godfrey

Investigation: Samantha Godfrey

Data Curation: Samantha Godfrey

Writing – Original Draft Preparation: Samantha Godfrey

Writing – Review & Editing: Samantha Godfrey, Andrew Plater, James Cooper

Visualization: Samantha Godfrey

Supervision: Andrew Plater, James Cooper

Project Administration: Samantha Godfrey

Funding Acquisition: Andrew Plater

Conflicts of Interest

The authors declare no conflicts of interest.

Institutional Review Board Statement

Not Applicable

Informed Consent Statement

Not Applicable

Data Availability Statement

The data that support the findings of this study are available from the corresponding author upon reasonable request.

References

Agisoft. (2018). Agisoft PhotoScan User Manual Professional Edition, Version 1.4. Retrieved from https://www.agisoft.com/downloads/user-manuals/

Brasington, J., Vericat, D. & Rychkov, I. (2012). Modeling river bed morphology, roughness, and surface sedimentology using high resolution terrestrial laser scanning. Water Resources Research, 48(11). https://doi.org/10.1029/2012WR012223

Casella, E., Drechsel, J., Winter, C., Benninghoff, M. & Rovere, A. (2020). Accuracy of sand beach topography surveying by drones and photogrammetry. Geo-Marine Letters, 255–268. https://doi.org/10.1007/s00367-020-00638-8

Castillo, C., Pérez, R., James, M. R., Quinton, J. N., Taguas, E. V. & Gómez, J. A. (2012). Comparing the Accuracy of Several Field Methods for Measuring Gully Erosion. Soil Science Society of America Journal, 76(4), 1319–1332. https://doi.org/10.2136/sssaj2011.0390

Del Río, L., Posanski, D., Gracia, F.J. *(2020).* A comparative approach of monitoring techniques to assess erosion processes on soft cliffs. *Bull Eng Geol Environ* **79,** 1797–1814. https://doi.org/10.1007/s10064-019-01680-2" https://doi.org/10.1007/s10064-019-01680-2

Dewez, T. J. B., Rohmer, J., Regard, V. & Cnudde, C. (2013). Probabilistic coastal cliff collapse hazard from repeated terrestrial laser surveys: case study from Mesnil Val (Normandy, northern France). Journal of Coastal Research, 65. https://doi.org/10.2112/SI65-119.1

Duffy, J., Shutler, J., Witt, M., DeBell, L., Anderson, K., Duffy, J. P. & Anderson, K. (2018). Tracking Fine-Scale Structural Changes in Coastal Dune Morphology Using Kite Aerial Photography and Uncertainty-Assessed Structure-from-Motion Photogrammetry. Remote Sensing, 10(9), 1494. https://doi.org/10.3390/rs10091494

Eltner, A., Kaiser, A., Castillo, C., Rock, G., Neugirg, F. & Abellán, A. (2016). Image-based surface reconstruction in geomorphometry; merits, limits and developments. Earth Surface Dynamics, 4(2), 359–389. https://doi.org/10.5194/esurf-4-359-2016

Eltner, A. & Schneider, D. (2015). Analysis of Different Methods for 3D Reconstruction of Natural Surfaces from Parallel-Axes UAV Images. The Photogrammetric Record, 30(151), 279–299. https://doi.org/10.1111/phor.12115

Environment Agency. (2019). National Coastal Erosion Risk Mapping. Retrieved July 3, 2020, from https://environment.maps.arcgis.com/apps/webappviewer/index.html?id=9cef4a084bbb4954b970cd35b099d94c

Godfrey, S., Cooper, J., Bezombes, F., & Plater, A. (2020). Monitoring coastal morphology: the potential of low-cost fixed array action cameras for 3D reconstruction. *Earth Surface Processes and Landforms*, esp.4892. https://doi.org/10.1002/esp.4892

Gruen, A. (2012). Development and Status of Image Matching in Photogrammetry. Photogrammetric Record, 27(137), 36–57. https://doi.org/10.1111/j.1477-9730.2011.00671.x

Harley, M. D., Turner, I. L., Short, A. D. & Ranasinghe, R. (2011). A reevaluation of coastal embayment rotation: The dominance of cross-shore versus alongshore sediment transport processes, Collaroy-Narrabeen Beach, southeast Australia. Journal of Geophysical Research: Earth Surface, 116(4). https://doi.org/10.1029/2011JF001989

James, M. R. & Robson, S. (2012). Straightforward reconstruction of 3D surfaces and topography with a camera: Accuracy and geoscience application. Journal of Geophysical Research: Earth Surface, 117(F3), n/a-n/a. https://doi.org/10.1029/2011JF002289

James, M. R., Robson, S. & Smith, M. W. (2017). 3-D uncertainty-based topographic change detection with structure-from-motion photogrammetry: precision maps for ground control and directly georeferenced surveys. Earth Surface Processes and Landforms, 42(12), 1769–1788. https://doi.org/10.1002/esp.4125

JNCC. (2019). Unmanned Aerial Vehicles for use in marine monitoring. Marine Monitoring Platform Guidelines No. 3., 1–30. Retrieved from http://data.jncc.gov.uk

Letortu, P., Jaud, M., Grandjean, P., Ammann, J., Costa, S., Maquaire, O. & Delacourt, C. (2018). Examining high-resolution survey methods for monitoring cliff erosion at an operational scale. GIScience and Remote Sensing, 55(4), 457–476. https://doi.org/10.1080/15481603.2017.1408931

Moore, R. D., Wolf, J., Souza, A. J. & Flint, S. S. (2009). Morphological evolution of the Dee Estuary, Eastern Irish Sea, UK: A tidal asymmetry approach. Geomorphology, 103(4), 588–596. https://doi.org/10.1016/j.geomorph.2008.08.003

Nagle-McNaughton, T & Cox, R. (2020). Measuring Change Using Quantitative Differencing of Repeat Structure-From-Motion Photogrammetry: The Effect of Storms on Coastal Boulder Deposits. Remote Sensing 12, no. 1: 42. https://doi.org/10.3390/rs12010042

Nouwakpo, S. K., Weltz, M. A. & McGwire, K. (2016). Assessing the performance of structure-from-motion photogrammetry and terrestrial LiDAR for reconstructing soil surface microtopography of naturally vegetated plots. Earth Surface Processes and Landforms, 41(3), 308–322. https://doi.org/10.1002/esp.3787

Pikelj, K., Ružić, I., Ilić, S., James, M. R. & Kordić, B. (2018). Implementing an efficient beach erosion monitoring system for coastal management in Croatia. Ocean and Coastal Management, 156, 223–238. https://doi.org/10.1016/j.ocecoaman.2017.11.019

Plater, A. J., & Grenville, J. (2010). Liverpool Bay: Linking the eastern Irish Sea to the Sefton Coast. In A. T. Worsley, G. Lymbery, V. J. C. Holden, & M. Newton (Eds.), Sefton's Dynamic Coast (pp. 28-54). Ainsdale-on-Sea, Southport: Coastal Defence: Sefton MBC Technical Services Department.

Prosdocimi, M., Calligaro, S., Sofia, G., Dalla Fontana, G. & Tarolli, P. (2015). Bank erosion in agricultural drainage networks: new challenges from structure-from-motion photogrammetry for post-event analysis. Earth Surface Processes and Landforms, 40(14), 1891–1906. https://doi.org/10.1002/esp.3767

Rosser, N. J., Brain, M. J., Petley, D. N., Lim, M. & Norman, E. C. (2013). Coastline retreat via progressive failure of rocky coastal cliffs. Geology, 41(8), 939–942. https://doi.org/10.1130/G34371.1

Rossi, R. (2018). Evaluation of `Structure-from-Motion' from a Pole-Mounted Camera for Monitoring Geomorphic Change. All Graduate Theses and Dissertations. Retrieved from https://digitalcommons.usu.edu/etd/6924

Smith, M. W. & Vericat, D. (2015). From experimental plots to experimental landscapes: topography, erosion and deposition in sub-humid badlands from Structure-from-Motion photogrammetry. Earth Surface Processes and Landforms, 40(12), 1656–1671. https://doi.org/10.1002/esp.3747

Streckel, B. & Koch, R. (2005). Lens model selection for visual tracking. Lecture Notes in Computer Science, 3663, 41–48. https://doi.org/10.1007/11550518_6

Visser, F., Woodget, A., Skellern, A., Forsey, J., Warburton, J. & Johnson, R. (2019). An evaluation of a low-cost pole aerial photography (PAP) and structure from motion (SfM) approach for topographic surveying of small rivers. International Journal of Remote Sensing, 40(24), 9321–9351. https://doi.org/10.1080/01431161.2019.1630782

Warrick, J. A., Ritchie, A. C., Adelman, G., Adelman, K. & Limber, P. W. (2017). New Techniques to Measure Cliff Change from Historical Oblique Aerial Photographs and Structure-from-Motion Photogrammetry. Journal of Coastal Research, 33(1), 39. https://doi.org/10.2112/jcoastres-d-16-00095.1

Wessling, R., Maurer, J. & Krenn-Leeb, A. (2014). Structure from Motion for Systematic Single Surface Documentation of Archaeological Excavations.

Westoby, M. J., Lim, M., Hogg, M., Pound, M. J., Dunlop, L. & Woodward, J. (2018). Cost-effective erosion monitoring of coastal cliffs. Coastal Engineering, 138, 152–164. https://doi.org/10.1016/J.COASTALENG.2018.04.008